

ARTICLE

Open Access

Low-dose real-time X-ray imaging with nontoxic double perovskite scintillators

Wenjuan Zhu¹, Wenbo Ma¹, Yirong Su¹, Zeng Chen², Xinya Chen¹, Yaoguang Ma¹, Lizhong Bai¹, Wenge Xiao¹, Tianyu Liu¹, Haiming Zhu², Xiaofeng Liu¹, Huafeng Liu¹, Xu Liu¹ and Yang (Michael) Yang¹

Abstract

X-rays are widely used in probing inside information nondestructively, enabling broad applications in the medical radiography and electronic industries. X-ray imaging based on emerging lead halide perovskite scintillators has received extensive attention recently. However, the strong self-absorption, relatively low light yield and lead toxicity of these perovskites restrict their practical applications. Here, we report a series of nontoxic double-perovskite scintillators of $\text{Cs}_2\text{Ag}_{0.6}\text{Na}_{0.4}\text{In}_{1-y}\text{Bi}_y\text{Cl}_6$. By controlling the content of the heavy atom Bi^{3+} , the X-ray absorption coefficient, radiative emission efficiency, light yield and light decay were manipulated to maximise the scintillator performance. A light yield of up to $39,000 \pm 7000$ photons/MeV for $\text{Cs}_2\text{Ag}_{0.6}\text{Na}_{0.4}\text{In}_{0.85}\text{Bi}_{0.15}\text{Cl}_6$ was obtained, which is much higher than that for the previously reported lead halide perovskite colloidal CsPbBr_3 (21,000 photons/MeV). The large Stokes shift between the radioluminescence (RL) and absorption spectra benefiting from self-trapped excitons (STEs) led to a negligible self-absorption effect. Given the high light output and fast light decay of this scintillator, static X-ray imaging was attained under an extremely low dose of $\sim 1 \mu\text{Gy}_{\text{air}}$, and dynamic X-ray imaging of finger bending without a ghosting effect was demonstrated under a low-dose rate of $47.2 \mu\text{Gy}_{\text{air}} \text{ s}^{-1}$. After thermal treatment at 85°C for 50 h followed by X-ray irradiation for 50 h in ambient air, the scintillator performance in terms of the RL intensity and X-ray image quality remained almost unchanged. Our results shed light on exploring highly competitive scintillators beyond the scope of lead halide perovskites, not only for avoiding toxicity but also for better performance.

Introduction

X-ray imaging has been actively utilised in the fields of industrial material inspection, medical diagnosis and scientific research^{1–10}. Low-dose irradiation, high stability and high spatial resolution are generally regarded as the most important characteristics for X-ray imaging^{11,12}. Current X-ray imaging systems mostly rely on scintillators that are capable of converting X-ray photons into visible photons that are then detected by a photodiode array^{13–15}. Conventional scintillators, such as thallium-doped caesium iodide (CsI:Tl)^{16,17} and cerium-doped lutetium–aluminium garnet

(LuAG:Ce)¹⁸, usually require expensive and time-consuming synthesis, which poses a major challenge for device processability. Unlike conventional scintillator materials, the emerging lead halide perovskites for X-ray detectors are starting to show attractive merits of facile fabrication, fast response and good spatial resolution^{19–26}. However, the relatively low X-ray light yield, lead toxicity^{27–29} and instability greatly limit their applications in high-end X-ray imaging featuring low-dose exposure, hazard-free manufacturing, real-time monitoring and robustness.

Fortunately, previous efforts have discovered many efficient lead-free emitters, e.g., double-perovskite^{30–32}, copper^{33–35} and bismuth (Bi)^{36–38}-based metal halides, which hold potential for X-ray scintillators. Very recently, Rb_2CuBr_3 ³³ and $\text{Cs}_2\text{NaTbCl}_6$ ³⁹ were shown to be scintillators with high light yield. However, the long decay time and strong afterglow impede their use in realising high

Correspondence: Yang (Michael) Yang (yangyang15@zju.edu.cn)

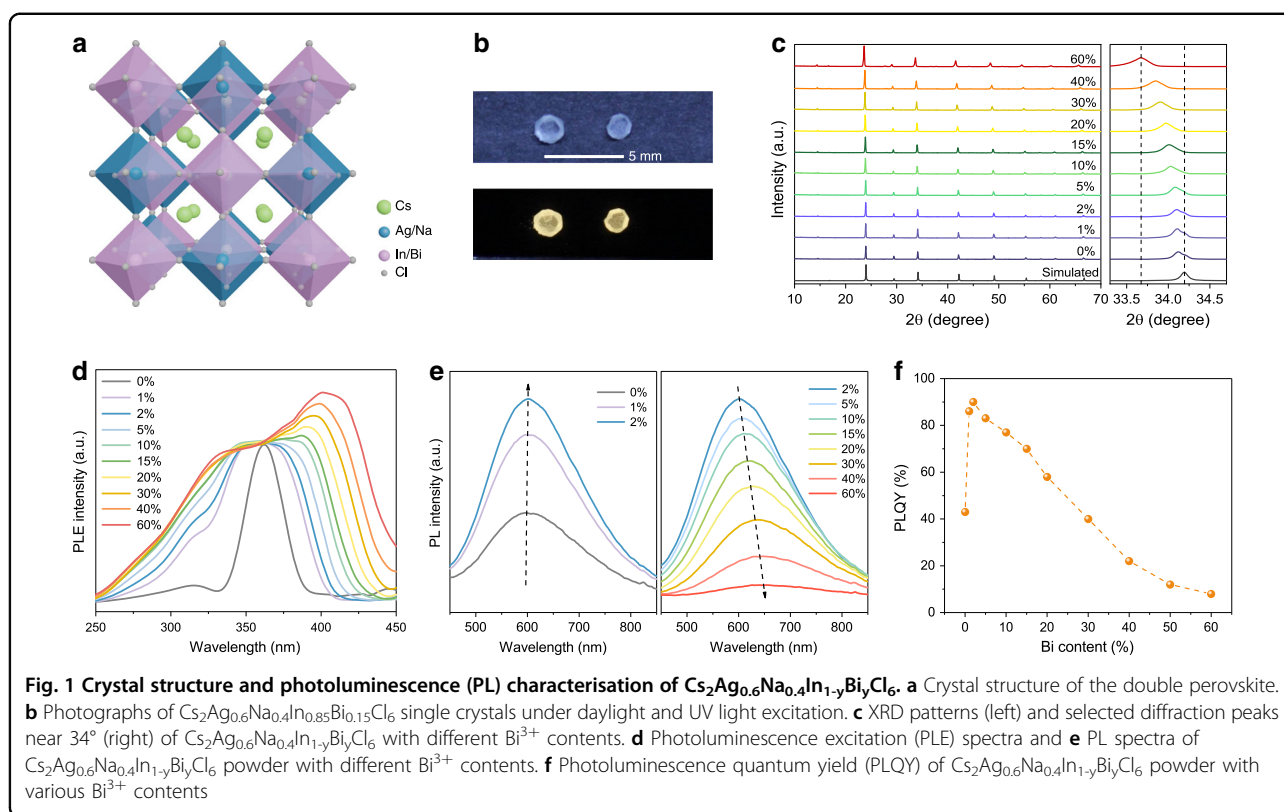
¹State Key Laboratory of Modern Optical Instrumentation, College of Optical Science and Engineering, International Research Center for Advanced Photonics, Zhejiang University, Hangzhou, Zhejiang, China

²Center for Chemistry of High-Performance & Novel Materials, department of Chemistry, Zhejiang University, Hangzhou, Zhejiang, China
These authors contributed equally: Wenjuan Zhu, Wenbo Ma

© The Author(s) 2020



Open Access This article is licensed under a Creative Commons Attribution 4.0 International License, which permits use, sharing, adaptation, distribution and reproduction in any medium or format, as long as you give appropriate credit to the original author(s) and the source, provide a link to the Creative Commons license, and indicate if changes were made. The images or other third party material in this article are included in the article's Creative Commons license, unless indicated otherwise in a credit line to the material. If material is not included in the article's Creative Commons license and your intended use is not permitted by statutory regulation or exceeds the permitted use, you will need to obtain permission directly from the copyright holder. To view a copy of this license, visit <http://creativecommons.org/licenses/by/4.0/>.



contrast X-ray imaging, especially for X-ray computed tomography (CT). Another limitation of Rb_2CuBr_3 is that its emission wavelength is in the blue region, which does not match the peak response of the common camera. Hence, the development of nontoxic halide scintillators with merits of high light yield, fast light decay and well-matched emission wavelength remains a challenge. In this article, a series of nontoxic double perovskites of $\text{Cs}_2\text{Ag}_{0.6}\text{Na}_{0.4}\text{In}_{1-y}\text{Bi}_y\text{Cl}_6$ single crystals with variable Bi^{3+} content were prepared. The introduction of a moderate amount of Bi^{3+} not only improves the radioluminescence (RL) output but also accelerates the radiative recombination, leading to a high scintillator light yield of $39,000 \pm 7000$ photons/MeV and fast light decay for $\text{Cs}_2\text{Ag}_{0.6}\text{Na}_{0.4}\text{In}_{0.85}\text{Bi}_{0.15}\text{Cl}_6$. The nontoxic scintillator delivers long-term stability under continuous thermal treatment and X-ray irradiation in ambient air. With a $\text{Cs}_2\text{Ag}_{0.6}\text{Na}_{0.4}\text{In}_{0.85}\text{Bi}_{0.15}\text{Cl}_6$ wafer as the scintillator, high-quality static and dynamic images of different objects were obtained under low-dose X-ray irradiation.

Results

Commonly, the double-perovskite structure $\text{Cs}_2\text{B}^{\text{I}}\text{B}^{\text{III}}\text{Cl}_6$ is regarded as a homologue of the ABX_3 -type perovskite, in which the B sites are replaced by equal amounts of monovalent and trivalent cations⁴⁰. Herein, B^{I} is occupied by Ag^+ and Na^+ with different alloying ratios.

By means of Na^+ doping in $\text{Cs}_2\text{AgInCl}_6$, the parity-forbidden transition is partly broken, and the electronic dimensionality is reduced as well³¹. Therefore, bright near-white light emission via radiative recombination of self-trapped excitons (STEs) of $\text{Cs}_2\text{Ag}_{1-x}\text{Na}_x\text{InCl}_6$ ($x = 0.2, 0.4, 0.6, 0.8$) single crystals is obtained. The optimised Na^+ content x is determined to be 0.4, for which the photoluminescence quantum yield (PLQY) reaches 43% (Supplementary Fig. S1).

Bi is an earth-abundant and green element, and it has an even larger atomic number than the widely used heavy X-ray absorbing elements of Pb and Tl; hence, we introduced partial Bi^{3+} to replace In^{3+} , initially for the purpose of increasing the X-ray absorption efficiency^{41,42}. The powder X-ray diffraction (PXRD) patterns of a series of $\text{Cs}_2\text{Ag}_{0.6}\text{Na}_{0.4}\text{In}_{1-y}\text{Bi}_y\text{Cl}_6$ (Fig. 1c) samples confirm that the pure double-perovskite phase is the same as $\text{Cs}_2\text{AgInCl}_6$, which belongs to space group $Fm\bar{3}m$ with a face-centred cubic structure. It is worth mentioning that the PXRD peaks shift to a lower diffraction angle with increasing Bi^{3+} content due to the larger ionic radius of Bi^{3+} (103 pm) than that of In^{3+} (80 pm), which can be clearly observed in the zoomed-in figure (right side of Fig. 1c). In addition, the scanning electron microscopy–energy-dispersive spectrometry (SEM–EDS) results (Supplementary Table S2) of six averaged random spots on the testing sample demonstrate that the final chemical compositions of

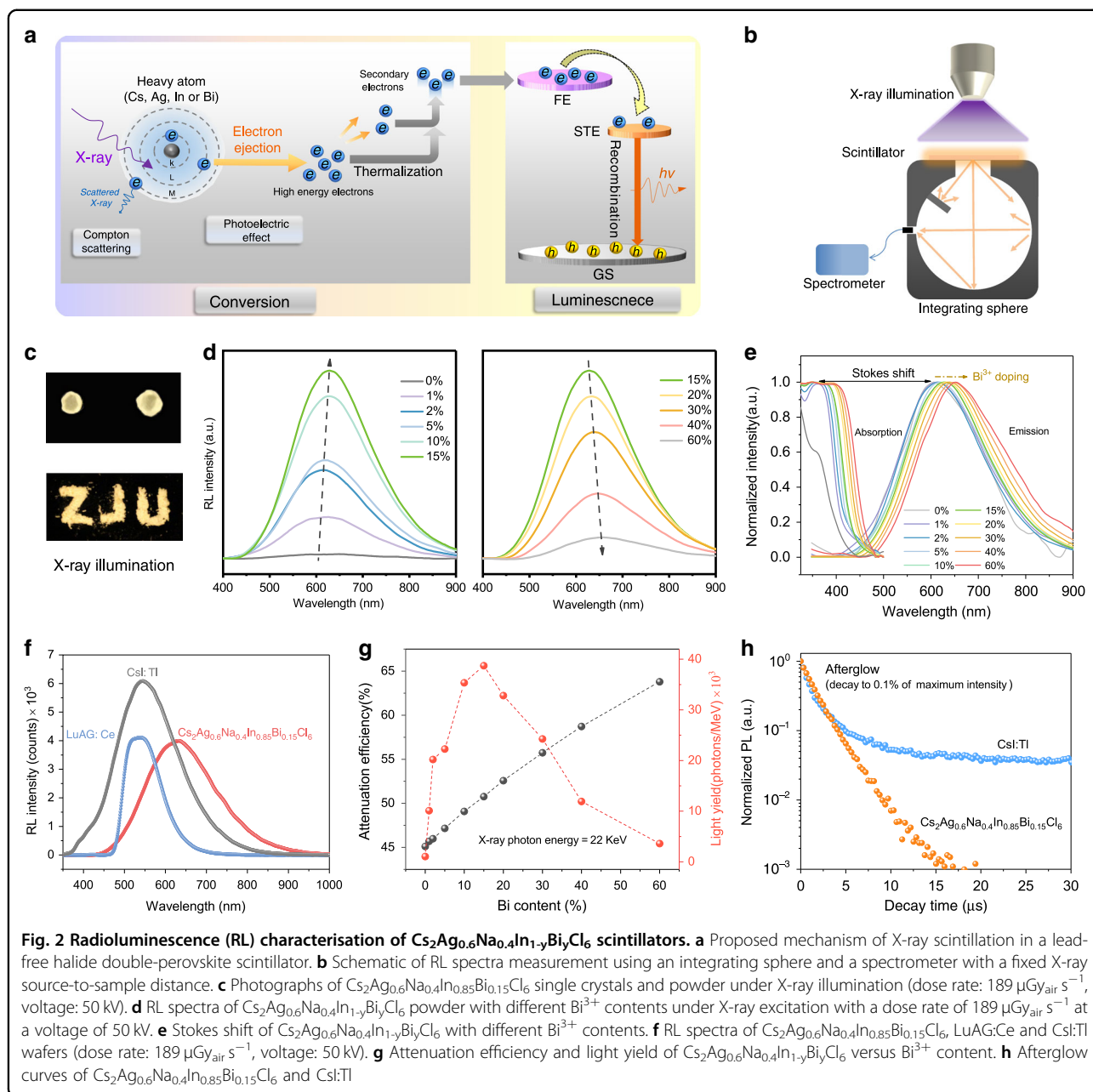
$\text{Cs}_2\text{Ag}_{0.6}\text{Na}_{0.4}\text{In}_{1-y}\text{Bi}_y\text{Cl}_6$ agree with the designed ratios. All the above analyses suggest that alloyed compounds of $\text{Cs}_2\text{Ag}_{0.6}\text{Na}_{0.4}\text{In}_{1-y}\text{Bi}_y\text{Cl}_6$ are successfully synthesised, whose chemical components change regularly, depending on the Bi/In ratio.

Interestingly, in addition to the expected enhancement of the X-ray absorption, the luminescence properties of the alloyed double perovskites can also be tuned by Bi^{3+} alloying. The photoluminescence excitation (PLE) peak near 362 nm becomes more distinct and broader as the Bi^{3+} content increases (Fig. 1d), which is consistent with the steady-state absorption spectra (Supplementary Fig. S2). To evaluate the absorption band tail width of $\text{Cs}_2\text{Ag}_{0.6}\text{Na}_{0.4}\text{In}_{1-y}\text{Bi}_y\text{Cl}_6$, we calculated the Urbach energy (E_U) from the plotted straight fitting lines, and the corresponding values are given (Supplementary Fig. S2). Compared with $\text{Cs}_2\text{Ag}_{0.6}\text{Na}_{0.4}\text{InCl}_6$, the E_U of the Bi^{3+} -doped perovskites significantly decreases, demonstrating that the band tail can be effectively suppressed because of further breaking of the parity-forbidden transition by the incorporated Bi^{3+} ^{43–45}. When introducing more Bi^{3+} , the absorption peak at 362 nm widens gradually and becomes less clear, and its intensity increases and is finally saturated in agreement with the PLE spectra, suggesting multiple absorption states that are widely distributed. The incorporated Bi^{3+} contributes to the valence-band structure by introducing shallow states right above the valence-band maximum of $\text{Cs}_2\text{Ag}_{0.6}\text{Na}_{0.4}\text{In}_{1-y}\text{Bi}_y\text{Cl}_6$ ³¹ and forming a hyperfine energy level³⁰, leading to broad absorption and excitation. Meanwhile, the absorption edges redshift as the Bi/In ratio increases, and the bandgap (E_g) values were calculated from Tauc plots (Supplementary Fig. S3), demonstrating that the bandgap is monotonically decreasing⁴⁶. Figure 1e shows the PL spectra of $\text{Cs}_2\text{Ag}_{0.6}\text{Na}_{0.4}\text{In}_{1-y}\text{Bi}_y\text{Cl}_6$ as a function of Bi^{3+} content. The PL intensity rapidly intensifies when the Bi^{3+} concentration increases from 0 to 2% and then weakens with further doping of Bi^{3+} , obtaining the highest PLQY of 90% (Fig. 1f). Meanwhile, the PL peak redshifts from 605 nm to 652 nm due to the gradually narrowed bandgap caused by the Bi^{3+} substitution of In^{3+} , in agreement with the absorption spectra. Apparently, the PL and absorption spectra overlap for this double-perovskite system is negligible. The large Stokes shift avoids the self-absorption effect that is detrimental to the output of scintillation light¹⁴. Both the outstanding PL efficiency and negligible self-absorption of $\text{Cs}_2\text{Ag}_{0.6}\text{Na}_{0.4}\text{In}_{1-y}\text{Bi}_y\text{Cl}_6$ imply that these materials have the potential to be good scintillators.

The light decay time is another figure of merit for scintillators. The TRPL of $\text{Cs}_2\text{Ag}_{0.6}\text{Na}_{0.4}\text{In}_{1-y}\text{Bi}_y\text{Cl}_6$ was obtained by the TCSPC method pumped with a femtosecond laser (400 nm, <300 fs, 1 MHz). As shown in Supplementary Fig. S4, the decay curve of $\text{Cs}_2\text{Ag}_{0.6}\text{Na}_{0.4}\text{InCl}_6$

can be fitted by a biexponential function, giving a fast decay process (~1 ns) and a slower decay process (2.8 μs), which is assigned to the forbidden STE emission³⁰. To investigate the origin of the fast decay process, the TRPL of the STE-emission band (we used a filter to selectively collect the light signal from 700 nm to 800 nm) was monitored, and it still showed distinct fast decay (Supplementary Fig. S5), excluding the possibility of band-to-band radiative recombination. This fast component gradually vanishes with the incorporation of Bi^{3+} . Hence, the fast decay process (~1 ns) may be assigned to the defect trapping process^{30,45} since Bi^{3+} can passivate defects³¹. In addition, when collecting the TRPL with different time resolutions (4 ps/16 ps/512 ps), the fast decay process becomes unobvious when the time resolution is 512 ps (Supplementary Fig. S5), indicating that this ultrafast process cannot be detected with low time resolution. With increasing Bi^{3+} content, the lifetime of the slow component gradually shortens to the nanosecond level, which is superior to that of the current commercial Cs:TI¹⁶, demonstrating the great potential for dynamic real-time X-ray imaging. We reason that the breaking of the parity-forbidden transition induced by Bi^{3+} doping results in improved radiative recombination kinetics; therefore, the lifetime becomes shorter.

To assess the scintillation property, a series of $\text{Cs}_2\text{Ag}_{0.6}\text{Na}_{0.4}\text{In}_{1-y}\text{Bi}_y\text{Cl}_6$ were tested under X-ray illumination. Figure 2a shows a plausible mechanism of X-ray scintillation in the lead-free halide double perovskites. The radiation energy is first absorbed by the heavy atoms of the double perovskites mainly through the photoelectric effect and inelastic Compton scattering, ejecting massive hot electrons; then, these electrons thermalise on an ultrafast timescale and are captured by luminescent centres^{47,48}. The high PLQY of our double-perovskite ensures that once electrons transfer to the recombination centre, the ultimate radiative emission is very efficient. To accurately measure the RL, equimolecular $\text{Cs}_2\text{Ag}_{0.6}\text{Na}_{0.4}\text{In}_{1-y}\text{Bi}_y\text{Cl}_6$ powder with various Bi ratios were compressed into compact wafers, and then, these wafers were closely attached to the circular window of an integrating sphere with a fixed distance to the X-ray source. The corresponding RL spectra were recorded by a fibre-coupled spectrometer (Fig. 2b). Figure 2c shows photographs of $\text{Cs}_2\text{Ag}_{0.6}\text{Na}_{0.4}\text{In}_{0.85}\text{Bi}_{0.15}\text{Cl}_6$ SCs and powder under X-ray excitation, yielding strong and uniform light-yellow emission. Figure 2d shows that the scintillation output has a nonmonotonic relation with the Bi ratio. It first increases, reaches the peak intensity at 15% Bi^{3+} , and then drops as the Bi^{3+} content further increases, which is mainly attributed to the collective effect of the X-ray absorption efficiency (Fig. 2g) and radiative emission efficiency that can be reflected by the PLQY (Fig. 1f). As we anticipated, the calculated X-ray attenuation efficiency



of $\text{Cs}_2\text{Ag}_{0.6}\text{Na}_{0.4}\text{In}_{1-y}\text{Bi}_y\text{Cl}_6$ enhances monotonically with Bi^{3+} doping because of the large atomic number of Bi^{3+} (Fig. 2g). Herein, when the Bi^{3+} content is increased from 0 to 2%, both the PLQY and X-ray absorption of $\text{Cs}_2\text{Ag}_{0.6}\text{Na}_{0.4}\text{In}_{1-y}\text{Bi}_y\text{Cl}_6$ improve, leading to a rapid increase in the RL intensity. With further doping of Bi^{3+} from 2% to 15%, the near-linear improvement of the X-ray absorption dominates the slowly declining radiative emission efficiency, as manifested by the PLQY, resulting in continuous enhancement of the RL intensity. With Bi^{3+} doping greater than 15%, the contribution of rapidly decreased PLQY exceeds that of the increased X-ray

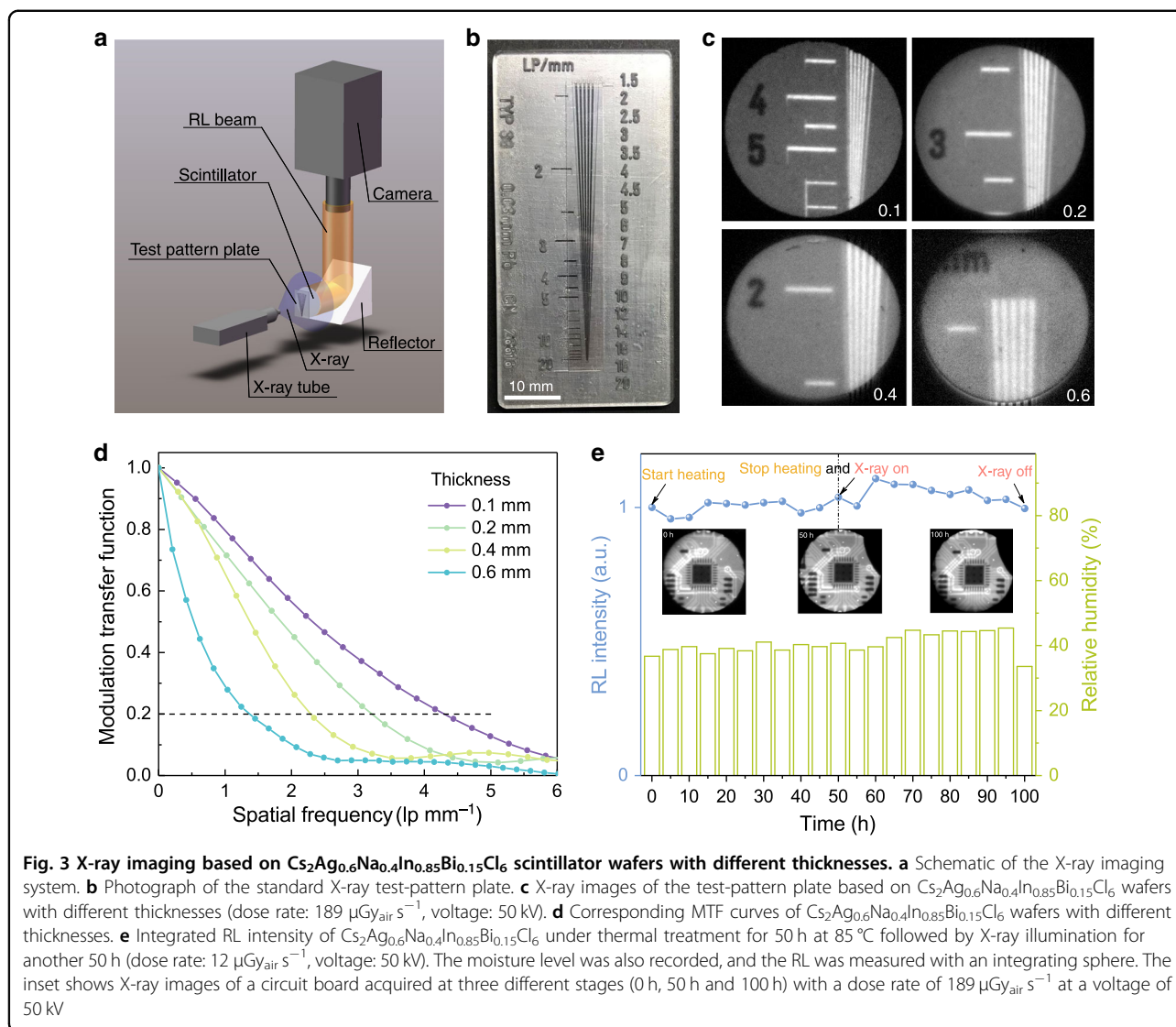
absorption efficiency of Bi^{3+} , and the overall RL intensity diminishes. The shapes of the RL spectra are consistent with those of the corresponding PL spectra, indicating that the last step of an X-ray scintillation event is the same as the PL process, that is, they both emit light through STEs. One unique feature of STE emission is that the absorption and RL peak have a large Stokes shift, leading to negligible self-absorption, while a Pb-based perovskite scintillator, e.g., CsPbBr_3 , has a very small Stokes shift due to its direct bandgap⁴. This large Stokes shift is generally favourable for any emitters but particularly desirable for scintillators since scintillators are very thick to ensure

sufficient absorption of X-rays, but the scintillations are usually weak¹⁴. As shown in Supplementary Fig. S6, the integrated RL intensity of $\text{Cs}_2\text{Ag}_{0.6}\text{Na}_{0.4}\text{In}_{0.85}\text{Bi}_{0.15}\text{Cl}_6$ has a linear response to the X-ray dose rate, highlighting its suitability for X-ray contrast imaging.

Equivalent to the PLQY, the light yield (LY) of a scintillator is regarded as the internal X-ray-to-photon conversion efficiency, which can be measured as the ratio of the total emitted photon number to the absorbed X-ray energy⁴⁷. Theoretically, the LY is governed by the relation $\text{LY} = 10^6 \times \text{SQ}/(\beta E_g)$, where β is a constant related to the host structure. As mentioned above, E_g slightly decreases with increasing Bi^{3+} content, which is a negligible factor for the LY in $\text{Cs}_2\text{Ag}_{0.6}\text{Na}_{0.4}\text{In}_{1-y}\text{Bi}_y\text{Cl}_6$. Hence, both the transfer efficiency S of hot-electron energy and the photoluminescence quantum yield Q (PLQY) govern the LY. In an attempt to quantify the RL light yield, we selected a commercial LuAG:Ce scintillator as a reference, whose light yield is $22,000 \pm 4000$ photons/MeV. To unify the absorbed X-ray energies of these two kinds of scintillator, the attenuation efficiencies of LuAG:Ce and $\text{Cs}_2\text{Ag}_{0.6}\text{Na}_{0.4}\text{In}_{0.85}\text{Bi}_{0.15}\text{Cl}_6$ as a function of thickness at an X-ray photon energy of 22 keV were calculated, since the major X-ray photon energy of our tube is 22 keV (Supplementary Fig. S7). Based on this relation curve, a $\text{Cs}_2\text{Ag}_{0.6}\text{Na}_{0.4}\text{In}_{0.85}\text{Bi}_{0.15}\text{Cl}_6$ wafer with a 0.4-mm thickness and a LuAG:Ce wafer with a 0.11-mm thickness were fabricated, and the corresponding RL spectra were recorded (Fig. 2f). In such circumstances, LuAG:Ce and $\text{Cs}_2\text{Ag}_{0.6}\text{Na}_{0.4}\text{In}_{0.85}\text{Bi}_{0.15}\text{Cl}_6$ have the same X-ray absorption cross sections, and therefore, the light output can be fairly compared. Finally, $\text{Cs}_2\text{Ag}_{0.6}\text{Na}_{0.4}\text{In}_{0.85}\text{Bi}_{0.15}\text{Cl}_6$ delivers a light yield of $39,000 \pm 7000$ photons per MeV, comparable with that of commercial CsI:Tl and much higher than that of the previously reported lead halide perovskite colloidal CsPbBr_3 (21,000 photons/MeV)³. In addition, the light yields of $\text{Cs}_2\text{Ag}_{0.6}\text{Na}_{0.4}\text{In}_{1-y}\text{Bi}_y\text{Cl}_6$ for various Bi^{3+} contents are given in Fig. 2g, whose evolution trend corresponds well with the RL output intensity. It is noted that the trend of the scintillator light yield with the Bi^{3+} doping ratio is not exactly the same as that of the PLQY; $\text{Cs}_2\text{Ag}_{0.6}\text{Na}_{0.4}\text{In}_{0.85}\text{Bi}_{0.15}\text{Cl}_6$ has the highest scintillation light yield, while $\text{Cs}_2\text{Ag}_{0.6}\text{Na}_{0.4}\text{In}_{0.98}\text{Bi}_{0.02}\text{Cl}_6$ has the best PLQY. This highlights the fact that optimisation of the scintillator performance cannot always follow the PLQY results since the PLQY only reflects the efficiency of the last step of a scintillation event, that is, the radiative emission of the thermalized electrons. In addition to the PLQY, the transfer efficiency S of hot-electron energy also plays a decisive role in the LY. Owing to the high atomic number of Bi, we speculate that there is a tight radius of the hot-electron distribution around Bi^{3+} in $\text{Cs}_2\text{Ag}_{0.6}\text{Na}_{0.4}\text{In}_{1-y}\text{Bi}_y\text{Cl}_6$, which is

beneficial to hot-electron energy transfer⁴⁸. The LY value is maximised when the Bi^{3+} doping is 15% due to the collective effect of S and Q , and the SQ product is optimised under this circumstance. Another interesting discovery is that the optimised $\text{Cs}_2\text{Ag}_{0.6}\text{Na}_{0.4}\text{In}_{0.85}\text{Bi}_{0.15}\text{Cl}_6$ scintillator shows strong X-ray absorption efficiency from ~ 36 keV to 60 keV, which is the region for common medical digital radiography (Supplementary Fig. S8). Another important parameter for scintillators is the afterglow, which can reduce the signal-to-noise ratio (SNR) of the X-ray imaging. To obtain high contrast imaging without lag, it is always desirable to reduce the afterglow, especially for CT imaging. As shown in Fig. 2h, the luminance signal of $\text{Cs}_2\text{Ag}_{0.6}\text{Na}_{0.4}\text{In}_{0.85}\text{Bi}_{0.15}\text{Cl}_6$ decays to 0.1% at ~ 16 μs . This low afterglow significantly outperforms that of the previous Rb_2CuBr_3 (2.72% @ 20 ms)³³ and is much lower than that of the widely used scintillator CsI:Tl (1.5% @ 3 ms), demonstrating the great potential of $\text{Cs}_2\text{Ag}_{0.6}\text{Na}_{0.4}\text{In}_{0.85}\text{Bi}_{0.15}\text{Cl}_6$ for real-time X-ray imaging and medical CT applications.

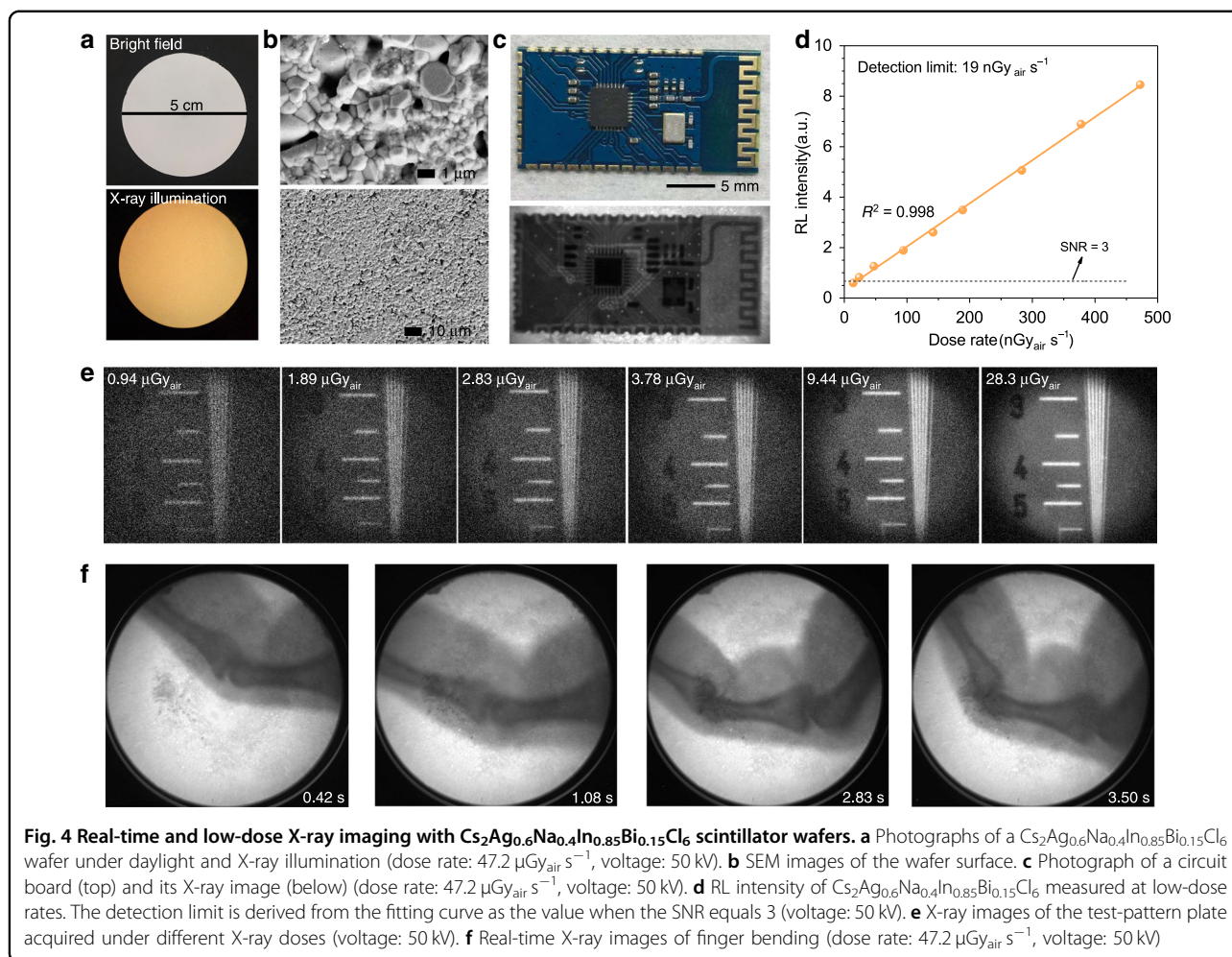
To implement X-ray imaging with $\text{Cs}_2\text{Ag}_{0.6}\text{Na}_{0.4}\text{In}_{0.85}\text{Bi}_{0.15}\text{Cl}_6$ as a scintillator, a homemade optical system was built, as illustrated in Fig. 3a. $\text{Cs}_2\text{Ag}_{0.6}\text{Na}_{0.4}\text{In}_{0.85}\text{Bi}_{0.15}\text{Cl}_6$ wafers with different thicknesses (0.1 mm, 0.2 mm, 0.4 mm and 0.6 mm) were tested for X-ray imaging performance. The X-ray images of the standard test-pattern plate given in Fig. 3c demonstrate that the spatial resolution decreases with thickening wafer due to the increased optical crosstalk caused by light scattering. To quantify the spatial resolution, the modulation transfer function (MTF) was calculated using slanted-edge images⁴⁹ (Supplementary Fig. S9). As shown in Fig. 3d, the spatial resolution (which is defined as the spatial frequency value at $\text{MTF} = 0.2$) is determined to be 4.3 lp mm^{-1} , 3.2 lp mm^{-1} , 2.3 lp mm^{-1} and 1.4 lp mm^{-1} for $\text{Cs}_2\text{Ag}_{0.6}\text{Na}_{0.4}\text{In}_{0.85}\text{Bi}_{0.15}\text{Cl}_6$ wafers with thicknesses of 0.1 mm, 0.2 mm, 0.4 mm and 0.6 mm, respectively, which are consistent with the values from the X-ray images of the standard test-pattern plate. The spatial resolution of the $\text{Cs}_2\text{Ag}_{0.6}\text{Na}_{0.4}\text{In}_{0.85}\text{Bi}_{0.15}\text{Cl}_6$ wafer with a 0.1-mm thickness is comparable with that of a Se direct-type X-ray imager (4.8 lp mm^{-1} at $\text{MTF} = 0.2$)^{2,50}. There is no doubt that further decreasing the thickness of the scintillator wafer can help improve the spatial resolution of X-ray imaging, but a larger dose rate will be needed to produce a sufficient scintillating light signal when taking real-time imaging⁵¹. It is also worth mentioning that the spatial resolution can be further enhanced if the scintillator screen is closely attached to the CMOS panel since the optical crosstalk will be minimised in this case. However, with such an optical configuration, the field of view (FOV) is restricted by the size of the very expensive CMOS chip, while with our optical setup, we can view large objects such as human fingers with a $13.2\text{-mm} \times 13.2\text{-mm}$ CMOS chip.



The environmental, thermal and X-ray radiation stability of the $\text{Cs}_2\text{Ag}_{0.6}\text{Na}_{0.4}\text{In}_{0.85}\text{Bi}_{0.15}\text{Cl}_6$ scintillator regarding the RL intensity and X-ray image quality was systematically investigated. XRD patterns of $\text{Cs}_2\text{Ag}_{0.6}\text{Na}_{0.4}\text{In}_{0.85}\text{Bi}_{0.15}\text{Cl}_6$ (Supplementary Fig. S10) measured after long-term exposure to humid ambient air indicate its high structural stability, which outperforms that of the known lead-based perovskites. The irradiation stability and thermostability of $\text{Cs}_2\text{Ag}_{0.6}\text{Na}_{0.4}\text{In}_{0.85}\text{Bi}_{0.15}\text{Cl}_6$ under ambient air were further examined. As shown in Fig. 3e, the RL intensity shows no obvious degradation under thermal treatment for 50 h at 85°C followed by continuous X-ray irradiation for another 50 h (Fig. 3e). The X-ray images of a circuit board acquired at three specific time points (0 h, 50 h and 100 h) can hardly be distinguished from each other (inset of Fig. 3e). In addition, the MTF values of the X-ray images acquired at 0 h, 50 h

and 100 h show only a slight variation (Supplementary Fig. S11). All the above analyses provide evidence of the excellent feasibility of applying the $\text{Cs}_2\text{Ag}_{0.6}\text{Na}_{0.4}\text{In}_{0.85}\text{Bi}_{0.15}\text{Cl}_6$ scintillator in pervasive environments.

Based on the optimised composition and thickness, a wafer of $\text{Cs}_2\text{Ag}_{0.6}\text{Na}_{0.4}\text{In}_{0.85}\text{Bi}_{0.15}\text{Cl}_6$ with a 0.1-mm thickness and a 5-cm diameter was prepared. SEM images of the wafer surface present its compactness and homogeneity (Fig. 4b). Utilising this wafer, we obtained X-ray images of the test-pattern plate under different doses of radiation (Fig. 4e), and the corresponding MTF results give resolutions ranging from 1.5 lp mm^{-1} to 4.4 lp mm^{-1} (Supplementary Fig. S12). This result demonstrates our scintillator's capability to acquire high-resolution imaging under an extremely low dose of $\sim 1 \mu\text{Gy}_{\text{air}}$, which is, to the best of our knowledge, the lowest dose requirement for perovskite-based X-ray imaging. The integrated RL



intensity of $\text{Cs}_2\text{Ag}_{0.6}\text{Na}_{0.4}\text{In}_{0.85}\text{Bi}_{0.15}\text{Cl}_6$ measured in the low-dose rate range presents an excellent linear response to the X-ray dose rate (Fig. 4d). The detection limit derived from the fitting curve when the SNR equals 3 is $19 \text{ nGy}_{\text{air}} \text{s}^{-1}$, which is much lower than the typical medical imaging dose. To assess the feasibility of using the $\text{Cs}_2\text{Ag}_{0.6}\text{Na}_{0.4}\text{In}_{0.85}\text{Bi}_{0.15}\text{Cl}_6$ scintillator for dynamic real-time X-ray imaging, a video of finger bending (Supplementary Video 1) was obtained under a low-dose rate of $47.2 \mu\text{Gy}_{\text{air}} \text{s}^{-1}$, which exhibits a distinct phase contrast without a ghosting effect. The randomly selected X-ray images from the video at different time points show obvious biological tissue phase contrast and clear joint details (Fig. 4f). Figure 4c and Supplementary Fig. S13 are high-quality X-ray images of different circuit boards with various electronic components. An X-ray image of the complete test-pattern plate is shown in Supplementary Fig. S14. Considering these X-ray imaging demonstrations, the $\text{Cs}_2\text{Ag}_{0.6}\text{Na}_{0.4}\text{In}_{0.85}\text{Bi}_{0.15}\text{Cl}_6$ scintillator qualifies as a potential candidate for low-dose real-time X-ray imaging.

Discussion

In conclusion, we developed a nontoxic $\text{Cs}_2\text{Ag}_{0.6}\text{Na}_{0.4}\text{In}_{0.85}\text{Bi}_{0.15}\text{Cl}_6$ double-perovskite scintillator, which exhibits not only a high light yield but also long-term stability under continuous thermal treatment and X-ray irradiation. High-resolution X-ray image attained under a low dose of $\sim 1 \mu\text{Gy}_{\text{air}}$ and distinct real-time imaging of finger bending demonstrate its great potential for X-ray imaging technology. Our results reveal the huge potential in exploring scintillators beyond lead halide perovskites, not only for avoiding toxic elements but also for achieving higher performance.

Methods

Sample fabrication and characterisation

A series of $\text{Cs}_2\text{Ag}_{1-x}\text{Na}_x\text{In}_{1-y}\text{Bi}_y\text{Cl}_6$ single crystals were prepared by a slightly modified hydrothermal reaction²⁸. First, 2 mmol of CsCl (99.9%, Xi'an Polymer Light Technology Corp.) was dissolved in 10 ml of a 10 M HCl (AR, Sinopharm) solution, followed by the addition of $1-x$ mol AgCl (99.999%, Aldrich), x mol NaCl (99.99%, Aladdin),

1- y mol InCl_3 (99.999%, Aldrich) and y mol BiCl_3 (99.99%, Macklin) at a certain ratio. The resulting mixture was transferred into a 50-ml Teflon autoclave and heated at 180 °C for 12 h. After cooling down to room temperature at 3 °C h^{-1} , the precipitated millimetre-scale crystals were washed with isopropanol several times and dried at 60 °C in a vacuum oven.

The scintillator wafers were compressed from ground powder of the resulting bulk crystals using a hydraulic press. Approximately 50–500 mg of the powder was pressed at 15 MPa for 5 min to form scintillator wafers with thicknesses in the range of 0.1–1 mm. The thickness of the wafers was measured by a thickness gauge.

X-ray diffraction (XRD) analyses were carried out after grinding crystals into fine powder on an X-pert Powder diffractometer (PANalytical B.V.) with $\text{Cu-K}\alpha$ radiation ($\lambda = 0.15405$ nm) in the 2θ range from 10° to 70°. Photoluminescence (PL) and PL excitation (PLE) spectra were recorded by an Edinburgh Instruments spectrofluorometer (FLS920). Scanning electron microscopy (SEM) images and energy-dispersive spectrometry (EDS) results were taken on a Hitachi SU8030 electron microscope equipped with an Oxford X-Max 20 silicon drift detector. Steady-state absorption spectra were detected using a home-built ultraviolet–visible spectrophotometer system equipped with an integrating sphere. PL quantum yield (PLQY) measurements were performed using an absolute photoluminescence measurement system (Hamamatsu Quantaaurus-QY). Time-resolved photoluminescence (TRPL) decay kinetics were collected using a time-correlated single photon counting (TCSPC) module (PicoHarp 300) and an SPAD detector (IDQ, id100). The sample was excited by a femtosecond laser (Light Conversion Pharos, 400 nm, <300 fs, 1 MHz). Afterglow curves were detected using the single shot transient digitiser (SSTD) technique. Radioluminescence (RL) spectra were measured by a fibre-coupled fluorescence spectrometer (Ocean Optics QE PRO) equipped with an integrating sphere and a fixed X-ray source-to-sample distance.

Light-yield measurement

As is known, the light yield can be regarded as the ratio of the number of photons emitted from the luminescent sites to the total absorbed X-ray energy. First, we separately calculated the attenuation efficiency of LuAG:Ce (22,000 \pm 4000 photons/MeV) and $\text{Cs}_2\text{Ag}_{0.6}\text{Na}_{0.4}\text{In}_{0.85}\text{Bi}_{0.15}\text{Cl}_6$ as a function of sample thickness at an X-ray photon energy of 22 keV. To unify the absorbed X-ray energies of these two kinds of scintillator, a $\text{Cs}_2\text{Ag}_{0.6}\text{Na}_{0.4}\text{In}_{0.85}\text{Bi}_{0.15}\text{Cl}_6$ wafer with a 0.4-mm thickness and a LuAG:Ce wafer with a 0.11-mm thickness were compressed. Then, the scintillator wafers were closely

attached to the circular window of an integrating sphere with a fixed distance to the X-ray source, and the corresponding RL spectra were recorded by a QE PRO fibre-coupled fluorescence spectrometer (carefully calibrated by an Ocean Optics engineer before usage). Comparing the integrated intensities of the two spectra, a light yield of 39,000 \pm 7000 photons/MeV for the $\text{Cs}_2\text{Ag}_{0.6}\text{Na}_{0.4}\text{In}_{0.85}\text{Bi}_{0.15}\text{Cl}_6$ scintillator was acquired. The measurement system was cross-checked with another commercial scintillator of CsI:TI , obtaining a light yield of 57,000 photons/MeV, which matches its datasheet value (\sim 60,000 photons/MeV) and proves the validity of the measurement method.

X-ray imaging optical system setup

A Mini-X X-ray tube (target material: Ag, $P_{\text{max}} = 4$ W, $V_{\text{max}} = 50$ kV, $I_{\text{max}} = 79$ μA) produced by Amptek Inc. was utilised as the X-ray source, generating an X-ray output spectrum with both intense characteristic radiation of Ag and broad bremsstrahlung radiation. The average X-ray photon energy was \sim 22 keV. The X-ray dose rates were altered by adjusting the current of the X-ray tube from 5 μA to 79 μA , and were calibrated by a highly sensitive X-ray ion chamber dose meter (Radcal Corporation 10 \times 5-180). The objects and scintillator wafers were placed vertically to the incident X-rays, and the scintillators were fixed just behind the objects. A reflector was utilised to deflect the optical path by 90° to diminish the negative influence caused by direct radiation from the X-ray source on the camera. To collect X-ray images, a CMOS camera (Photometrics 95B) with 1200 \times 1200 pixels and a 11- μm pixel size was equipped.

MTF measurements

MTF represents the capability to transfer the input signal modulation at a given spatial frequency to its output, and can be used to evaluate the fundamental spatial resolution performance of an imaging system. The spatial resolution can be determined by the spatial frequency value when $\text{MTF} = 0.2$. The MTF curve was calculated by the slanted-edge method. First, a piece of aluminium (thickness: \sim 1 mm) with a sharp edge was placed on the scintillator, and its edge profile was derived from the resulting X-ray image. Then, the edge spread function (ESF) was derived from the edge profile, from which we could deduce the line spread function (LSF). Finally, the MTF values were defined by the Fourier transform of the LSF as follows:

$$\text{MTF}(\nu) = F(\text{LSF}(x)) = F\left(\frac{d\text{ESF}(x)}{dx}\right),$$

where ν is the spatial frequency, and x is the position of the pixels.

Acknowledgements

The authors acknowledge the support from the National Key Research and Development Program of China (2017YFA0207700), Outstanding Youth Fund of Zhejiang Natural Science Foundation of China (LR18F050001) and National Natural Science Foundation of China (61804134, 61525106, U1809204). The authors would also like to thank Mr. Yufen Han and Mr. Suilao Yao of the Beijing Hamamatsu Photonics for their helpful discussions.

Author contributions

Y.(M.)Y. conceived the idea and supervised the project. Y.(M.)Y., W.Z. and W.M. designed the experiments. W.Z. carried out material preparation and characterisations. W.M., Y.(M.)Y. and Y.M. set up the X-ray imaging system. W.M. and W.Z. measured the scintillator property and implemented the X-ray imaging experiments. Z.C. conducted the PL-decay measurement. Y.S. and X.C. assisted the X-ray imaging experiments. W.X. and X.L. helped in the PLQY measurement. L.B. and T.L. assisted the compressing of wafers and absorption spectra measurement. W.Z. wrote the first draft of the paper and Y.(M.)Y. revised the paper with comments from X.L., H.L. and all other authors.

Conflict of interest

The authors declare that they have no conflicts of interest.

Supplementary information is available for this paper at <https://doi.org/10.1038/s41377-020-00353-0>.

Received: 6 March 2020 Revised: 12 June 2020 Accepted: 17 June 2020

Published online: 30 June 2020

References

- Chen, Q. S. et al. All-inorganic perovskite nanocrystal scintillators. *Nature* **561**, 88–93 (2018).
- Heo, J. H. et al. High-performance next-generation perovskite nanocrystal scintillator for nondestructive X-ray imaging. *Adv. Mater.* **30**, 1801743 (2018).
- Zhang, Y. H. et al. Metal halide perovskite nanosheet for X-ray high-resolution scintillation imaging screens. *ACS Nano* **13**, 2520–2525 (2019).
- Wang, L. L. et al. Ultra-stable CsPbBr₃ perovskite nanosheets for X-ray imaging screen. *Nano-Micro Lett.* **11**, 52 (2019).
- Cao, F. et al. Shining emitter in a stable host: design of halide perovskite scintillators for X-ray imaging from commercial concept. *ACS Nano* **14**, 5183–5193 (2020).
- Kim, Y. C. et al. Printable organometallic perovskite enables large-area, low-dose X-ray imaging. *Nature* **550**, 87–91 (2017).
- Van Eijk, C. W. E. Inorganic scintillators in medical imaging. *Phys. Med. Biol.* **47**, R85–R106 (2002).
- Chapman, H. N. et al. Femtosecond X-ray protein nanocrystallography. *Nature* **470**, 73–77 (2011).
- Lecoq, P. Development of new scintillators for medical applications. *Nucl. Instrum. Methods Phys. Res. Sect. A: Accelerators, Spectrometers, Detect. Associated Equip.* **809**, 130–139 (2016).
- Rabin, O. et al. An X-ray computed tomography imaging agent based on long-circulating bismuth sulphide nanoparticles. *Nat. Mater.* **5**, 118–122 (2006).
- Spahn, M. X-ray detectors in medical imaging. *Nucl. Instrum. Methods Phys. Res. Sect. A: Accelerators, Spectrometers, Detect. Associated Equip.* **731**, 57–63 (2013).
- Rowlands, J. A. Material change for X-ray detectors. *Nature* **550**, 47–48 (2017).
- Yaffe, M. J. & Rowlands, J. A. X-ray detectors for digital radiography. *Phys. Med. Biol.* **42**, 1–39 (1997).
- Greskovich, C. & Duclos, S. Ceramic scintillators. *Annu. Rev. Mater. Sci.* **27**, 69–88 (1997).
- Büchle, P. et al. X-ray imaging with scintillator-sensitized hybrid organic photodetectors. *Nat. Photonics* **9**, 843–848 (2015).
- Wang, Z. G. et al. Kinetic Monte Carlo simulations of excitation density dependent scintillation in CsI and CsI (Tl). *Phys. Status Solidi B* **250**, 1532–1540 (2013).
- Nillius, P. et al. Light output measurements and computational models of microcolumnar CsI scintillators for x-ray imaging. *Med. Phys.* **42**, 600–605 (2015).
- Xu, J. et al. Fabrication, microstructure, and luminescent properties of Ce³⁺-Doped Lu₃Al₅O₁₂(Ce:LuAG) transparent ceramics by low-temperature vacuum sintering. *J. Am. Ceram. Soc.* **96**, 1930–1936 (2013).
- Yakunin, S. et al. Detection of X-ray photons by solution-processed lead halide perovskites. *Nat. Photonics* **9**, 444–449 (2015).
- Shrestha, S. et al. High-performance direct conversion X-ray detectors based on sintered hybrid lead triiodide perovskite wafers. *Nat. Photonics* **11**, 436–440 (2017).
- Kawano, N. et al. Scintillating organic-inorganic layered perovskite-type compounds and the gamma-ray detection capabilities. *Sci. Rep.* **7**, 14754 (2017).
- Wei, W. et al. Monolithic integration of hybrid perovskite single crystals with heterogenous substrate for highly sensitive X-ray imaging. *Nat. Photonics* **11**, 315–321 (2017).
- Birowosuto, M. D. et al. X-ray scintillation in lead halide perovskite crystals. *Sci. Rep.* **6**, 37254 (2016).
- Wang, X. et al. PIN diodes array made of perovskite single crystal for X-ray imaging. *Phys. Status Solidi RRL* **12**, 1800380 (2018).
- Liu, J. Y. et al. Flexible, printable soft-X-ray detectors based on all-inorganic perovskite quantum dots. *Adv. Mater.* **31**, 1901644 (2019).
- Mykhaylyk, V. B., Kraus, H. & Saliba, M. Bright and fast scintillation of organolead perovskite MAPbBr₃ at low temperatures. *Mater. Horiz.* **6**, 1740–1747 (2019).
- Jiang, T. M. et al. Power conversion efficiency enhancement of low-bandgap mixed Pb-Sn perovskite solar cells by improved interfacial charge transfer. *ACS Energy Lett.* **4**, 1784–1790 (2019).
- Gao, Y. et al. Highly stable lead-free perovskite field-effect transistors incorporating linear π -conjugated organic ligands. *J. Am. Chem. Soc.* **141**, 15577–15585 (2019).
- Jiang, T. M. et al. Realizing high efficiency over 20% of low-bandgap Pb-Sn alloyed perovskite solar cells by in situ reduction of Sn⁴⁺. *Sol. RRL* **4**, 1900467 (2020).
- Yang, B. et al. Lead-free direct band gap double-perovskite nanocrystals with bright dual-color emission. *J. Am. Chem. Soc.* **140**, 17001–17006 (2018).
- Luo, J. J. et al. Efficient and stable emission of warm-white light from lead-free halide double perovskites. *Nature* **563**, 541–545 (2018).
- Volonakis, G. et al. Cs₃InAgCl₆: a new lead-free halide double perovskite with direct band gap. *J. Phys. Chem. Lett.* **8**, 772–778 (2017).
- Yang, B. et al. Lead-free halide Rb₂CuBr₃ as sensitive X-ray scintillator. *Adv. Mater.* **31**, 1904711 (2019).
- Lin, R. C. et al. All-inorganic Cs₂Cu₂I₃ single crystal with high-PLQY (\approx 15.7%) intrinsic white-light emission via strongly localized 1D excitonic recombination. *Adv. Mater.* **31**, 1905079 (2019).
- Jun, T. et al. Lead-free highly efficient blue-emitting Cs₃Cu₂I₅ with 0D electronic structure. *Adv. Mater.* **30**, 1804547 (2018).
- Xie, J. L. et al. New lead-free perovskite Rb₂BiCl₆ nanocrystals with blue luminescence and excellent moisture-stability. *Nanoscale* **11**, 6719–6726 (2019).
- McCall, K. M. et al. From 0D Cs₃Bi₂I₉ to 2D Cs₃Bi₂I₆Cl₃: dimensional expansion induces a direct band gap but enhances electron–phonon coupling. *Chem. Mater.* **31**, 2644–2650 (2019).
- Ding, N. et al. Europium-doped lead-free Cs₃Bi₂Br₉ perovskite quantum dots and ultrasensitive Cu²⁺ detection. *ACS Sustain. Chem. Eng.* **7**, 8397–8404 (2019).
- Hu, Q. S. et al. X-ray scintillation in lead-free double perovskite crystals. *Sci. China Chem.* **61**, 1581–1586 (2018).
- Slavney, A. H. et al. A bismuth-halide double perovskite with long carrier recombination lifetime for photovoltaic applications. *J. Am. Chem. Soc.* **138**, 2138–2141 (2016).
- Steele, J. A. et al. Photophysical pathways in highly sensitive Cs₂AgBiBr₆ double-perovskite single-crystal X-ray detectors. *Adv. Mater.* **30**, 1804450 (2018).
- Pan, W. C. et al. Cs₂AgBiBr₆ single-crystal X-ray detectors with a low detection limit. *Nat. Photonics* **11**, 726–732 (2017).
- Meng, W. W. et al. Parity-forbidden transitions and their impact on the optical absorption properties of lead-free metal halide perovskites and double perovskites. *J. Phys. Chem. Lett.* **8**, 2999–3007 (2017).
- Han, P. G. et al. Size effect of lead-free halide double perovskite on luminescence property. *Sci. China Chem.* **62**, 1405–1413 (2019).

45. Hu, Q. S. et al. Tunable color temperatures and efficient white emission from $\text{Cs}_2\text{Ag}_{1-x}\text{Na}_x\text{In}_{1-y}\text{Bi}_y\text{Cl}_6$ double perovskite nanocrystals. *Small* **15**, 1903496 (2019).
46. Zhou, J. et al. Manipulation of $\text{Bi}^{3+}/\text{In}^{3+}$ transmutation and Mn^{2+} -doping effect on the structure and optical properties of double perovskite $\text{Cs}_2\text{NaBi}_{1-x}\text{In}_x\text{Cl}_6$. *Adv. Optical Mater.* **7**, 1801435 (2019).
47. Blasse, G. Scintillator materials. *Chem. Mater.* **6**, 1465–1475 (1994).
48. Grim, J. Q. et al. The roles of thermalized and hot carrier diffusion in determining light yield and proportionality of scintillators. *Phys. Status Solidi A* **209**, 2421–2426 (2012).
49. Samei, E., Flynn, M. J. & Reimann, D. A. A method for measuring the pre-sampled MTF of digital radiographic systems using an edge test device. *Med. Phys.* **25**, 102–113 (1998).
50. Kabir, M. Z. Effect of repeated x-ray exposure on the resolution of amorphous selenium based x-ray imagers. *Med. Phys.* **37**, 1339–1349 (2010).
51. Yasuda, R., Katagiri, M. & Matsubayashi, M. Influence of powder particle size and scintillator layer thickness on the performance of $\text{Gd}_2\text{O}_2\text{S}:\text{Tb}$ scintillators for neutron imaging. *Nucl. Instrum. Methods Phys. Res. Sect. A: Accelerators, Spectrometers, Detect. Associated Equip.* **680**, 139–144 (2012).